Nanoscale Horizons

ROYAL SOCIETY OF CHEMISTRY

COMMUNICATION

View Article Online
View Journal | View Issue

Cite this: *Nanoscale Horiz.*, 2025, **10**, 1159

Received 24th February 2025,
Accepted 31st March 2025

DOI: 10.1039/d5nh00107b

rsc.li/nanoscale-horizons

Reinforced supercapacitor electrode *via* reduced graphene oxide encapsulated $NiTe_2$–$FeTe_2$ hollow nanorods†

Mohammad Ali Saghafizadeh,[a] Akbar Mohammadi Zardkhoshoui*[b] and Saied Saeed Hosseiny Davarani *[a]

Metal telluride-based nanomaterials have garnered considerable interest as positive electrode materials for supercapacitors due to their plentiful redox-active sites, robust chemical stability, and excellent electrical conductivity. In this work, these advantageous properties are further enhanced by hybridizing $NiTe_2$–$FeTe_2$ (NFT) hollow nanorods with reduced graphene oxide (RGO), resulting in an NFT@RGO composite suitable for supercapacitor applications. The hollow rod-like structure promotes efficient ion diffusion and maximizes the exposure of electroactive sites, while the RGO network boosts conductivity and mitigates nanomaterial agglomeration, thus preserving structural integrity and prolonging material durability. The NFT@RGO-based electrode exhibits a notable capacity of 1388.5 C g^{-1} at 1 A g^{-1}, with 93.82% capacity retention after 10 000 cycles. This remarkable performance arises from the synergistic contributions of the Ni and Fe metals, the electrically conductive Te element, the RGO framework, and the unique hollow morphology of the nanorods. Furthermore, a hybrid device employing activated carbon (AC) as the negative electrode (NFT@RGO//AC) achieves an energy density of 61.11 W h kg^{-1} and retains 89.85% of its capacity over 10 000 cycles, underscoring the promise of NFT@RGO for next-generation supercapacitors. These findings position the designed nanomaterial as an excellent candidate for high-performance energy storage systems.

New concepts

This research introduces an effective approach to supercapacitor electrode design through the synthesis of $NiTe_2$–$FeTe_2$ (NFT) hollow nanorods encapsulated within a reduced graphene oxide matrix (NFT@RGO). The key innovation lies in the unique structural and compositional design, which synergistically enhances electrochemical performance through several mechanisms: (i) hollow nanorod architecture: the hollow structure of the NFT nanorods is a critical innovation, as it significantly increases the electrode's active surface area, facilitating greater ion accessibility and faster ion diffusion. This design also accommodates volume changes during charge–discharge cycles, thereby improving cycling stability and durability, (ii) integration of RGO with the NFT composite: the encapsulation of the hollow nanorods within the RGO matrix is a strategic innovation that enhances electrical conductivity and structural integrity. The RGO matrix not only provides a conductive network but also prevents aggregation of the nanorods, ensuring efficient electron transport. Additionally, the presence of Te in the composite introduces a synergistic effect, further enhancing conductivity and redox activity, which are crucial for high-performance supercapacitors, (iii) optimized electrode architecture: the combination of hollow nanorods and RGO creates a hierarchical structure that maximizes the utilization of active materials while minimizing ion diffusion paths. This optimized architecture results in superior rate capability, high specific capacity, and long-term cycling stability, addressing the limitations of traditional supercapacitor materials, (iv) mechanistic insights: the study provides a detailed mechanistic understanding of how the hollow nanorod structure and RGO encapsulation work in tandem to enhance electrochemical performance. The hollow structure reduces the diffusion resistance for ions, while the RGO matrix ensures rapid electron transfer, collectively leading to improved energy and power densities. These innovations position the NFT@RGO composite as a transformative material for bridging the performance gap between batteries and supercapacitors. By combining high energy density, excellent rate capability, and exceptional durability, this design offers a scalable and efficient energy storage solution for high-demand applications.

1. Introduction

The sustained development of human civilization fundamentally depends on the availability and utilization of energy. In particular, rising environmental concerns have created an urgent need for eco-friendly, highly efficient renewable energy sources.[1,2] Nonetheless, the inherent intermittency of most renewable options, such as tidal and solar power, impedes their continuous usage.[3,4] Consequently, the deployment of robust energy

[a] *Department of Chemistry, Shahid Beheshti University, G. C., 1983963113, Evin, Tehran, Iran. E-mail: ss-hosseiny@sbu.ac.ir; Fax: +98 21 22431661; Tel: +98 21 22431661*

[b] *Department of Chemical Technologies, Iranian Research Organization for Science and Technology (IROST), Tehran 3313193685, Iran. E-mail: A_mohammadi@irost.ir; Fax: +98 21 56276265; Tel: +98 21 56276283*

† Electronic supplementary information (ESI) available: Supplementary characterization and electrochemical data, and a benchmark table to compare the performance of as-prepared device with previous reported. See DOI: https://doi.org/10.1039/d5nh00107b

storage technologies is vital for maximizing the benefits of renewable energy. Among various storage devices, batteries and supercapacitors have been widely investigated. Supercapacitors, in particular, offer several advantages over conventional batteries, including minimal safety risks, rapid charging, low maintenance requirements, high power density, and superior longevity.[5–12] Despite these benefits, supercapacitors often exhibit drawbacks such as narrow voltage windows, complex redox behavior, and lower energy density compared to batteries.[13–15] According to the energy density equation [$E = 1/2 \times CV^2$], increasing both capacity and operating voltage can improve energy density.[16–18] Two strategies have emerged to address this limitation. The first involves elevating the operating voltage by constructing hybrid supercapacitors, which integrate the swift charging of supercapacitors with the higher energy storage capacity of batteries.[19,20] Since electrode materials, especially positive electrode materials have a decisive impact on device performance, much effort has focused on optimizing these components.[21–25] The second approach centers on designing innovative electrode materials characterized by low internal resistance, high redox activity, large surface areas, and favorable nanoarchitectures to enhance supercapacitor capacity.[26–28] Employing both strategies simultaneously offers the most comprehensive solution for boosting energy density.

Numerous studies have explored different positive electrode materials for hybrid supercapacitors. Metal oxides and hydroxides are widely examined owing to their abundance, cost-effectiveness, and straightforward synthesis methods.[29,30] However, their relatively low electrical conductivity constrains ion transport and reduces overall capacity.[31,32] Recent advances thus emphasize metal chalcogenides, including sulfides and selenides, for their improved conductivity and electrochemical performance.[33–36] Among these, tellurium (Te) stands out for its superior electrical properties, arising from its lower electronegativity compared to sulfur and selenium.[37,38] As a result, metal tellurides display enhanced physical, chemical, and electrochemical characteristics, largely due to a higher electronic conductivity of $\sim$10 000 S m^{-1}, far exceeding that of sulfur (5×10^{-28} S m^{-1}) and selenium (1 mS m^{-1}), which accelerates ion diffusion and bolsters electrochemical performance.[19,21] While singlet tellurium exhibits relatively low electrical conductivity compared to nickel metal, the formation of metal tellurides such as $NiTe_2$ and $FeTe_2$ results in materials with significantly enhanced conductivity. This is due to the metallic nature of these compounds and the synergistic interaction between the metal and tellurium atoms. In contrast, nickel oxide (NiO), a widely studied material for supercapacitors, has much lower conductivity due to its semiconducting nature. The high conductivity of metal tellurides, combined with their redox activity and structural stability, makes them ideal candidates for high-performance energy storage applications. For instance, our group synthesized $NiTe_2$@$CoTe_2$ *via* hydrothermal and tellurization techniques, achieving a substantial capacity of 1388.9 C g^{-1} and sustaining 96.67% capacity retention,[19] while Shi *et al.* employed a metal–organic framework strategy to produce $NiTe_2$@$CoTe_2$, resulting in a capacity of 941.04 C g^{-1}.[39]

Improving supercapacitor performance also heavily relies on the structural design of the nanomaterials employed. Recently, hollow or porous architectures have garnered considerable interest due to their high surface area and superior electrode–electrolyte interactions, which collectively enhance supercapacitive efficiency.[40–45] Several pioneering studies have reported the successful fabrication of hollow telluride-based nanostructures with promising electrochemical outcomes. Our team, for example, developed hollow FeNiCoTe nanocubes *via* a self-templating process, demonstrating improved supercapacitor performance relative to solid nanocubes.[21] Likewise, we constructed $NiTe_2$-MnTe hollow nanospheres through a MOF-based approach, achieving higher capacities compared to their solid counterparts.[25]

Reduced graphene oxide (RGO) frameworks are crucial in supercapacitors due to their excellent electrical conductivity and large specific surface area, which facilitate efficient charge transfer and provide abundant electroactive sites.[46,47] However, the two-dimensional (2D) form of RGO often suffers from aggregation, which restricts ion transport and limits access to electroactive sites, thereby diminishing electrode functionality.[48] To address this challenge, three-dimensional (3D) RGO structures have been explored. These 3D architectures retain the high conductivity and surface area of RGO while preventing the aggregation of active materials, thereby enhancing both efficiency and long-term stability. The integration of RGO with $NiTe_2$–$FeTe_2$ nanorods is a strategic approach to address several challenges in supercapacitor electrode materials. RGO provides a highly conductive network that enhances electron transport, mitigates the aggregation of $NiTe_2$–$FeTe_2$ nanorods, and accommodates volume changes during cycling, thereby preserving structural integrity. Furthermore, the porous structure of RGO facilitates efficient ion diffusion and increases the electroactive surface area, maximizing the utilization of the redox-active $NiTe_2$–$FeTe_2$ nanorods. This synergistic combination results in a composite material with superior electrochemical performance, including high specific capacity, excellent rate capability, and remarkable cycling stability, as demonstrated in this work.

In this work, we introduce RGO-encapsulated $NiTe_2$–$FeTe_2$ hollow nanorods designed to capitalize on RGO's flexibility in accommodating volume changes during electrochemical cycling, promoting efficient electron transport and reducing nanomaterial agglomeration. Our experimental findings demonstrate that this composite harnesses the complementary strengths of RGO's conductive matrix and $NiTe_2$–$FeTe_2$'s high electroactivity to deliver significantly enhanced charge storage. In particular, the NFT@RGO//AC hybrid supercapacitor developed in our study showcases robust capacity, extended cycle life, and noteworthy energy efficiency. This innovation charts a promising path toward industrial-scale applications and underscores the potential of next-generation, high-efficiency energy storage systems.

2. Experimental

2.1. Materials

This study utilized several chemicals: polyvinylpyrrolidone (molecular weight approximately 40 000), nickel(II) acetate tetrahydrate

($Ni(OCOCH_3)_2{\cdot}4H_2O$), ethanol ($C_2H_6O$), iron(II) sulfate heptahydrate ($FeSO_4{\cdot}7H_2O$), and tellurium powder.

2.2. Synthesis of the NFT

To synthesize NFT, 750 mg of polyvinylpyrrolidone and 350 mg of $Ni(OCOCH_3)_2{\cdot}4H_2O$ were dissolved in 50 mL of C_2H_6O. This solution was heated to 80 °C and refluxed under magnetic stirring for 10 hours. The resultant product was separated *via* centrifugation. Then, 10 mg of the synthesized Ni precursor was redispersed in 1 mL of C_2H_6O (referred to as solution I). Concurrently, 20 mg of $FeSO_4{\cdot}7H_2O$ was dissolved in a 10 mL mixture of H_2O and C_2H_6O (referred to as solution II). These solutions were combined, allowed to age for 20 minutes at room temperature under nitrogen protection, then the mixture was centrifuged, washed with C_2H_6O, and dried in a vacuum oven. The NFT composite was synthesized *via* a tellurization process. Briefly, 10 mg of NiFeLDH and 20 mg of Te powder were placed in separate porcelain boats, with the Te powder positioned upstream of the NiFeLDH in the furnace. The boats were heated to 500 °C at a rate of 5 °C per minute and maintained at this temperature for 2 hours under a nitrogen atmosphere. The nitrogen atmosphere ensured an inert environment, preventing oxidation and facilitating the reaction between Te vapor and NiFeLDH. During heating, the Te powder sublimated, producing Te vapor that diffused into the NiFeLDH structure, replacing hydroxide groups with telluride ions and forming the NFT composite. This process was also conducted at 300 °C and 600 °C to produce NFT300 and NFT600, respectively.

2.3. Synthesis of the NFT@RGO

NFT@RGO was synthesized by annealing a mixture of NFT and graphene oxide. Initially, 40 mg of NFT was ultrasonically dispersed in 40 mL of H_2O. To this dispersion, 10 mL of a 5 mg mL^{-1} graphene oxide suspension was added and stirred for 7 hours. The resulting mixture was then collected by centrifugation and annealed at 500 °C for 4 hours in an argon environment to reduce the graphene oxide.

2.4. Characterizations

Morphological features and chemical composition were examined using field emission scanning electron microscopy (FE-SEM, TESCAN MIRA 3, operating at 15 kV, Czech Republic) with an energy dispersive X-ray spectroscopy (EDX) attachment and transmission electron microscopy (TEM, Philips CM200). The crystal phases were analyzed using X-ray diffraction (XRD, Philips X'Pert Pro diffractometer). Raman spectroscopy of the NFT@RGO composite was conducted using a Raman spectrometer equipped with a 785 nm laser excitation source. X-ray photoelectron spectroscopy (XPS, Thermo Scientific ESCALAB 250Xi with an Mg X-ray source) was employed to determine the valence states of nickel, iron, and tellurium in NFT@RGO. Porosity properties such as pore size distributions and surface area were quantified using nitrogen adsorption–desorption isotherms on a SSA-4300, employing the Barrett–Joyner–Halenda (BJH) and Brunauer–Emmett–Teller (BET) methods.

2.5. Electrochemical tests

Electrochemical properties of our electrodes were meticulously evaluated using a three-electrode system. This setup included a platinum wire as the counter electrode, a mercury/mercuric oxide (Hg/HgO) electrode as the reference, and a 6 M solution of potassium hydroxide (KOH) serving as the electrolyte. The working electrodes were prepared using a slurry coating process, where the slurry comprising poly(tetrafluoroethylene), acetylene black, and the active nanomaterial in a 1 : 1 : 8 mass ratio was uniformly dispersed in C_2H_6O. This mixture was then evenly applied to nickel foam substrates, subsequently dried and compressed under pressure to ensure cohesion.[49,50] Each electrode was loaded with a precise mass of 5.0 mg for subsequent testing. The capacity of the electrodes (CS, expressed in C g^{-1}) was calculated using the following equation:[51]

$$C = \frac{I \times \Delta t}{w} \tag{1}$$

where I represents the current in amperes, Δt is the discharging time in seconds, and w denotes the mass of the active material in the electrode in grams. Coulombic efficiency (CE) for the NFT@RGO and the hybrid NFT@RGO//AC was determined by the ratio of the discharge time (t_{di}) to the charge time (t_{ch}), providing a measure of the energy efficiency during charge and discharge cycles: [$CE = t_{di}/t_{ch}$].[52] For practical application assessments, NFT@RGO served as the positive electrode, and activated carbon (AC), selected for its mechanical stability, high conductivity, and porosity, was used as the negative electrode in constructing a hybrid device (NFT@RGO//AC).[53] Before assembly, both the NFT@RGO and AC electrodes were immersed in KOH electrolyte, and a cellulose paper was employed as a separator to prevent electrical short circuits.[53] The mass balancing of the electrodes, crucial for optimizing device performance, was calculated using the charge balance principle:[54]

$$C^+w^+ = C^-w^-\Delta V^- \tag{2}$$

where: w^+ and w^- represent the masses of the NFT@RGO and AC electrodes, respectively (units: g), C^+ is the specific capacity of the NFT@RGO positive electrode (units: C g^{-1}), reflecting its battery-like behavior, C^- is the specific capacitance of the AC negative electrode (units: F g^{-1}), reflecting its capacitor-like behavior, Δ^- is the voltage window of the AC electrode (units: V). This equation ensures that the total charge stored in the positive electrode ($Q^+ = C^+w^+$) matches the total charge stored in the negative electrode ($Q^- = C^-w^-\Delta V^-$), accounting for the distinct electrochemical behaviors of the two electrodes.[54] We obtained mass values of 5.0 mg for NFT@RGO and 37.40 mg for AC. The energy density (E, in W h kg^{-1}) and power density (P, in W kg^{-1}) of the hybrid device were computed as follows:[55]

$$E = \frac{I\int V\,dt}{W \times 3.6} \tag{3}$$

$$P = 3600 \times \frac{E}{\Delta t} \tag{4}$$

where $I\int V\mathrm{d}t$ represents the integral of the current over voltage during the discharge cycle, and W is the total mass of the active materials in the hybrid device.

3. Results and discussion

The synthesis of the NFT@RGO composite is illustrated in Fig. 1. Initially, rod-like Ni precursor nanostructures are prepared through an optimized precipitation method. These precursors serve as sacrificial templates, governing the final hollow morphology. Subsequent chemical transformation involves the introduction of Fe^{2+} ions into the reaction system, initiating a hydrolysis reaction that releases protons (H^+). These protons gradually etch the Ni precursor framework, dissolving it and releasing Ni^{2+} ions into the solution. The Ni^{2+} and Fe^{2+} ions then co-precipitate, forming an intermediate NiFeLDH phase. The tellurization step proceeds *via* an anion-exchange mechanism, where hydroxide (OH^-) groups in the NiFeLDH lattice are replaced by telluride (Te^{2-}) anions, yielding the final $NiTe_2$–$FeTe_2$ (NFT) composite. To enhance electrochemical performance, the hollow NFT nanostructures are embedded within the RGO matrix. This conductive framework facilitates efficient electron transport while preventing nanoparticle aggregation, thereby optimizing charge-transfer kinetics and cycling stability.

The impact of the nanostructures' morphological evolution on their electrochemical efficiency was extensively analyzed using FESEM and TEM. The FESEM images, particularly Fig. 2a, highlight the rod-like morphology of the Ni precursors, while Fig. 2b confirms the rigidity of these structures. Post-hydrolysis, the rods maintain their morphology as evidenced in Fig. 2c. The transformation of the smooth surface into a hierarchical shell composed of oriented particles is vividly captured in Fig. 2d. EDX analysis further confirms the composition as NiFeLDH (Fig. S1, ESI†). During the tellurization process at varied temperatures (300, 500, and 600 °C), distinct morphological changes were observed. FESEM images of NFT300 show that while the structure retains the NiFeLDH morphology, it exhibits increased surface roughness (Fig. 2e), further detailed in Fig. 2f. At 500 °C, NFT500 maintains its rod-like form without noticeable aggregation (Fig. 2g), and the surface composed of ultrathin nanosheets is shown in Fig. 2h. EDX results for NFT500 confirm the presence of Te, Ni, and Fe, indicative of successful synthesis (Fig. S2, ESI†). However, increasing the temperature to 600 °C leads to structural degradation, evidenced by the collapse of the nanorods shown in Fig. 2i and j. FESEM images in Fig. 2k and l illustrate how NFT500, embedded within the RGO network, maintains its structural integrity and protects the nanostructures from degradation over prolonged cycling, thus enhancing electrochemical efficiency. EDX analysis of NFT500@RGO confirms the presence of Ni, Fe, C, Te, and O, validating the successful integration of these elements within the composite (Fig. S3, ESI†).

TEM analysis provides further insights into the morphology of these nanomaterials. Fig. 3a shows the TEM image of the Ni precursor, which demonstrates its rigid, rod-like structure devoid of pores an important feature for assessing the integrity of the fabricated material. Growth of particles on the surface of these rods is visible in Fig. 3b. Fig. 3c and d showcase the hollow nature of NFT500, with interconnected nanosheets creating a porous texture, likely enhancing ion transfer and

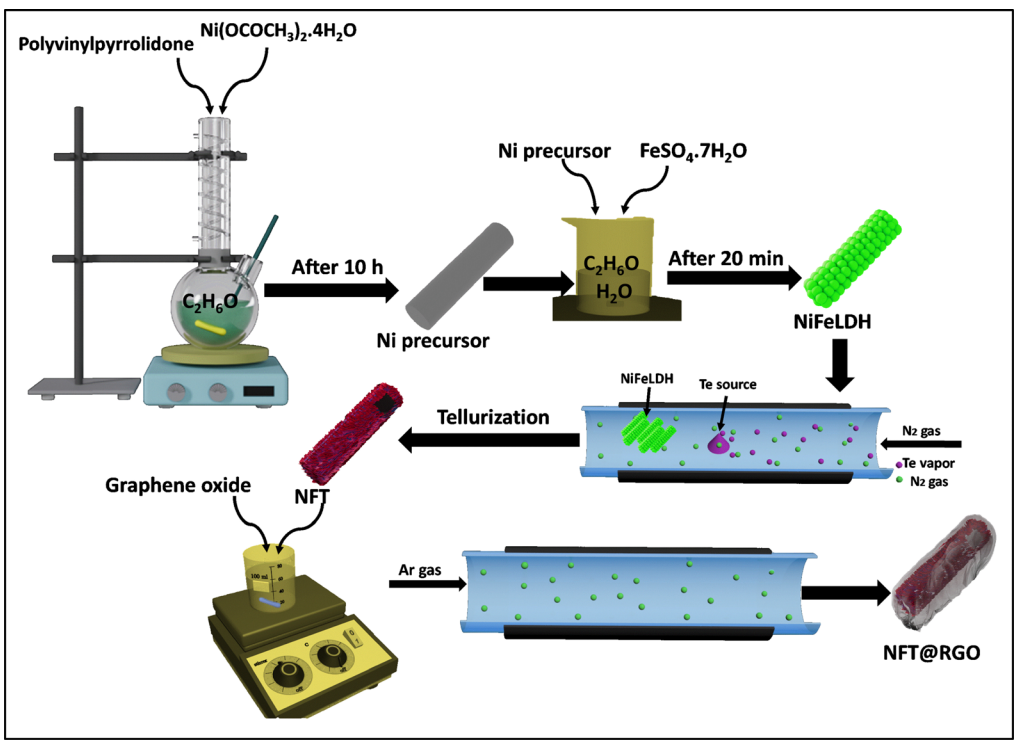

Fig. 1 Schematic for the fabrication of NFT@RGO.

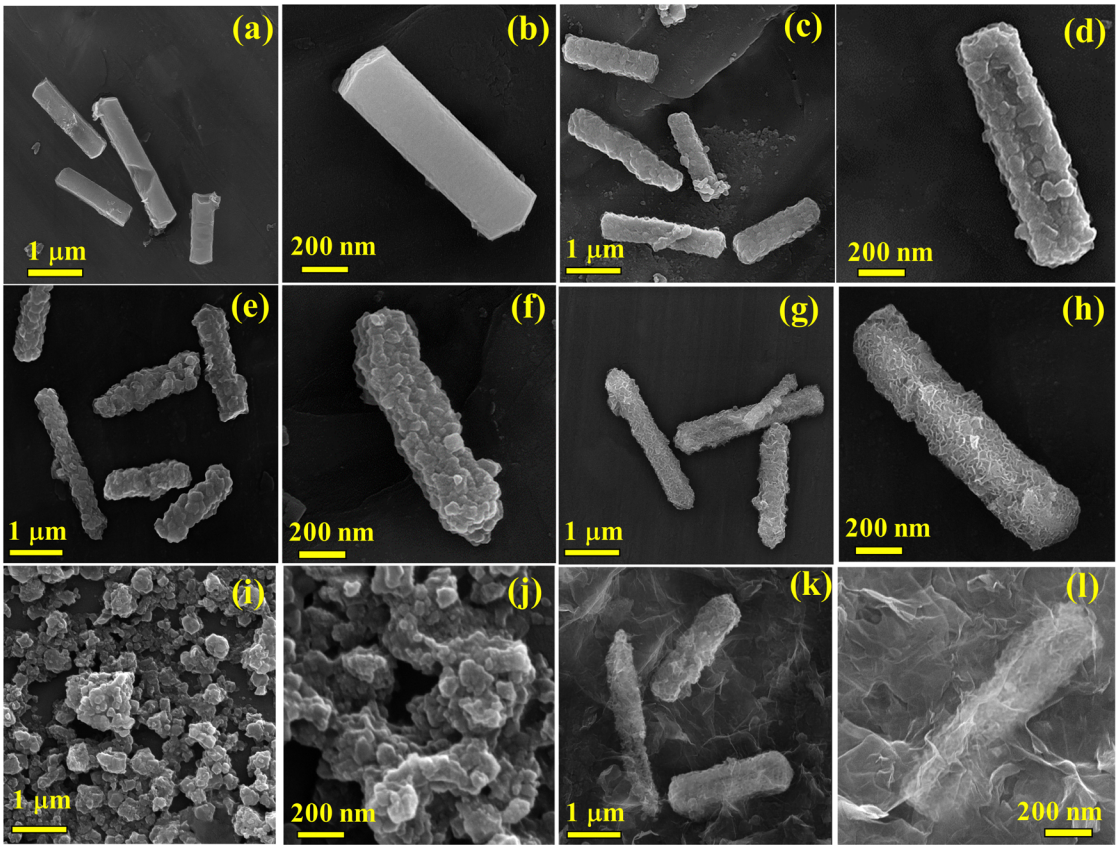

Fig. 2 (a and b) FESEM images of the Ni precursors. (c and d) FESEM images of the NiFeLDH. (e and f) FESEM images of the NFT300. (g and h) FESEM images of the NFT500. (i and j) FESEM images of the NFT600. (k and l) FESEM images of the NFT@RGO.

active surface area crucial for supercapacitor efficiency. The unique nanocomposite structure with RGO is highlighted in Fig. 3e and f, where NFT@RGO shows the nanoarchitectures wrapped in thin RGO layers, which not only protect the NFT from degradation but also contribute to the overall conductivity and performance of the material.[46,47] The design of the NFT composite introduces several innovative principles that distinguish it from previous studies. The combination of Ni and Fe in the telluride framework creates synergistic effects that enhance redox activity, electrical conductivity, and structural stability. These properties are further amplified by the hollow nanorod morphology, which provides a large electroactive surface area, accommodates volume changes during cycling, and promotes directional ion transport. The strategic integration of RGO forms a conductive network that enhances electron transport, prevents nanorod aggregation, and stabilizes the hollow structure. Together, these design principles result in a composite material (NFT@RGO) with exceptional electrochemical performance, including high specific capacity, excellent rate capability, and remarkable cycling stability. This work not only advances the field of supercapacitors but also provides a scalable and efficient solution for energy storage challenges.

The crystallinity of the synthesized nanomaterials was examined using X-ray diffraction (XRD), with the results displayed in Fig. 4a and Fig. S4 (ESI†). The XRD pattern of NiFeLDH align with previous literature, confirming its successful synthesis (Fig. S4, ESI†).[56,57] For the NFT@RGO, distinctive XRD signals corresponding to $FeTe_2$ (JCPDS no. 89-1639) and $NiTe_2$ (JCPDS no. 08-0004) phases are observed, as listed in Fig. 4a, validating the formation of these crystalline phases. The specific signals for $FeTe_2$ are found at several 2θ degrees, highlighting the detailed crystalline structure. Similarly, $NiTe_2$ exhibits XRD peaks at positions that confirm its crystalline phase, contributing to the overall structural framework of the composite.[58–61] An additional signal around 25°, observable in the XRD of the NFT500@RGO, implies the existence of the RGO, contributing to the nanocomposite's structural framework.[46,47] Raman spectroscopic analysis was employed to elucidate the compositional characteristics of the as-synthesized NFT@RGO composite. As illustrated in Fig. S5 (ESI†), the Raman spectrum exhibits distinct vibrational modes corresponding to the constituent phases. The peaks observed at approximately 83 and 139 cm^{-1} are attributed to the E_g and A_{1g} vibrational modes of $NiTe_2$, respectively.[62] Concurrently, two peaks at about 121 and 144 cm^{-1} are also associated with the A_g and B_{1g} vibrational modes of $FeTe_2$, confirming the presence of both bimetallic telluride phases.[63] Furthermore, the spectrum reveals two prominent peaks at 1347 and 1587 cm^{-1}, which are characteristic of the D band (disordered carbon) and G band (graphitic carbon) of RGO, respectively.[64] The co-existence of these vibrational

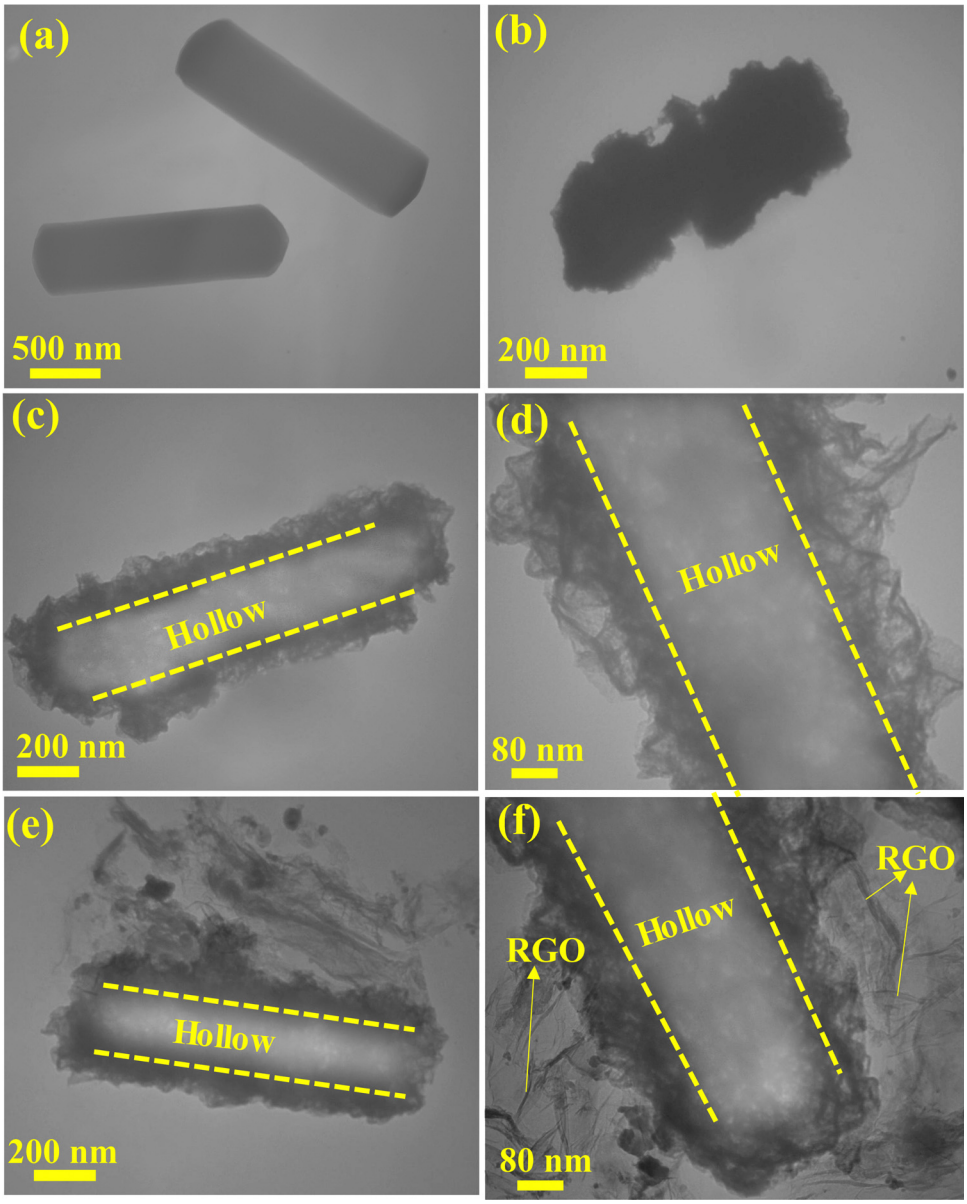

Fig. 3 (a) TEM image of the Ni precursors. (b) TEM image of the NiFeLDH. (c and d) TEM images of the NFT500. (e and f) TEM images of the NFT@RGO.

modes $NiTe_2$, $FeTe_2$, and RGO within the Raman spectrum of the NFT@RGO composite provides unequivocal evidence of the successful integration and coexistence of these components in the synthesized material. X-ray photoelectron spectroscopy (XPS) was employed to ascertain the oxidation states of Te, Ni, and Fe within the NFT500@RGO. The survey scan revealed in Fig. 4b shows the presence of Te, Fe, C, Ni, and O. Detailed analysis of the C 1s spectrum shows the transformation of GO to RGO, characterized by signals at 284.35 eV for C–C, 286.57 eV for C–O, 288.25 eV for C═O, and 288.92 eV for O–C═O (Fig. 4c).[65,66] This transformation is essential for enhancing the mechanical stability and electrical conductivity of the NFT500@RGO composite. The Ni 2p pattern discloses four distinguished signals, with those at the specific energies suggesting the presence of Ni^{2+} in the $2p_{3/2}$ (855.56 eV) and $2p_{1/2}$ (873.31 eV) states, alongside their satellite peaks (Fig. 4d).[67] The Fe 2p spectrum unveils signals at 722.12 and 708.73 eV, typical for the $2p_{1/2}$ and $2p_{3/2}$ states of Fe^{2+} (Fig. 4e).[68,69] In the Te 3d pattern, distinct peaks signify the $3d_{3/2}$ (583.84 eV) and $3d_{5/2}$ (572.90 eV) orbitals of the Te^{2-}, with additional signals indicating oxidation states because of the surface interactions (Fig. 4f).[70] Furthermore, the surface area and porosity, essential properties for supercapacitors, were evaluated using nitrogen adsorption–desorption isotherms. The isotherms for both NFT500 and NFT500@RGO exhibit type-IV characteristics with hysteresis loops indicative of mesoporosity.[46,47] Notably, NFT@RGO shows a significantly greater surface area (211 $m^2\ g^{-1}$) compared to NFT (113 $m^2\ g^{-1}$) and defined pore sizes of 7.7 and 9.6 nm, respectively (Fig. S6, ESI†), which are beneficial for enhancing the accessibility of electroactive sites and

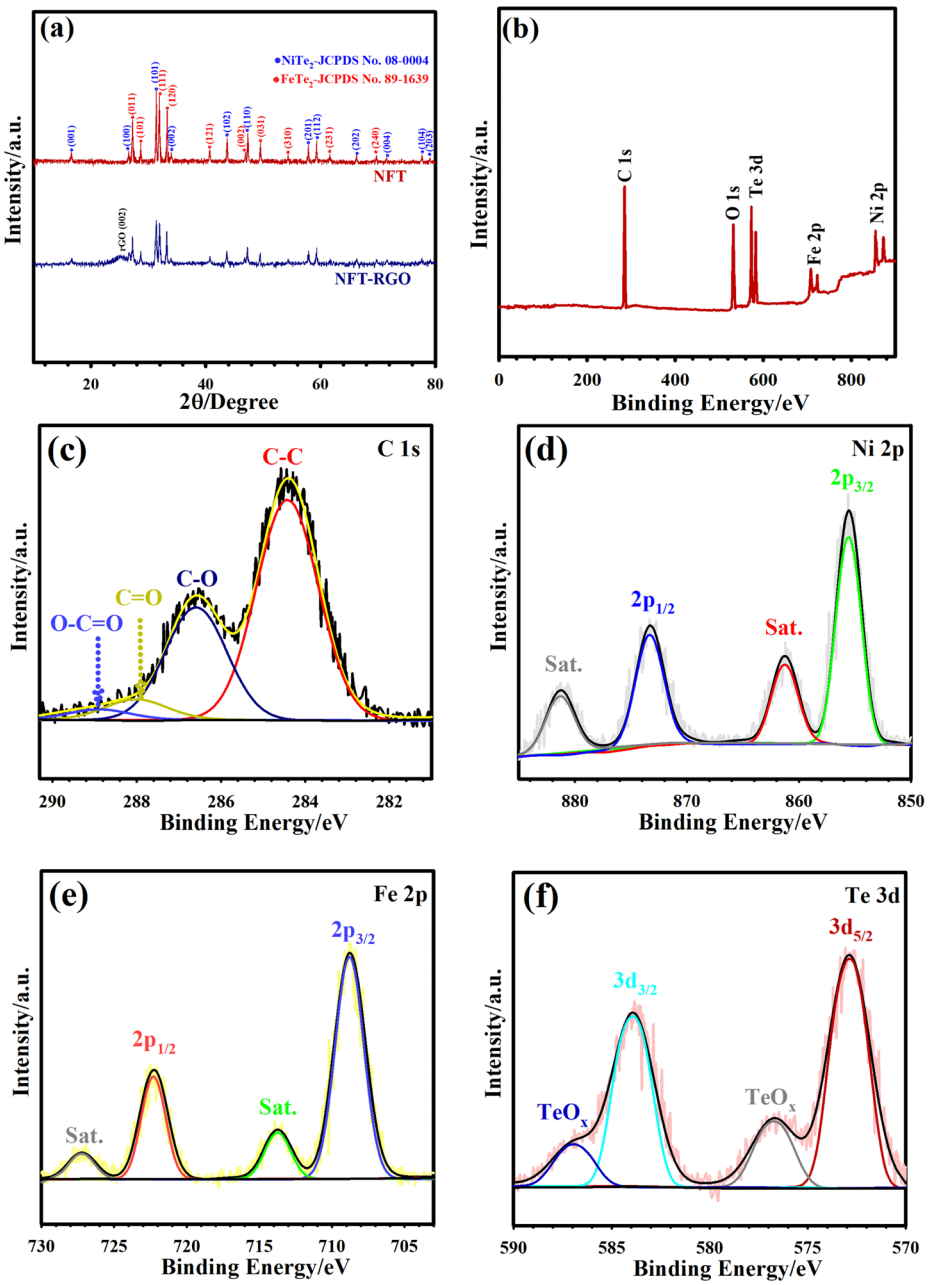

Fig. 4 (a) XRD patterns of the NFT@RGO and NFT500 samples. (b) Survey profile of the NFT@RGO. (c) C 1s XPS spectra of the NFT@RGO. (d) Ni 2p XPS spectra of the NFT@RGO. (e) Fe 2p XPS spectra of the NFT@RGO. (f) Te 3d XPS spectra of the NFT@RGO.

facilitating electron transfer, thus improving supercapacitor performance.[52]

The electrochemical performance of the electrodes was assessed using a three-electrode setup immersed in a 6 M KOH solution. The cyclic voltammetry (CV) profiles for NFT300, NFT500, and NFT600 were recorded at a scan rate of 10 mV s^{-1}, displayed in Fig. S7a (ESI†). Each profile showed distinctive redox peaks characteristic of faradaic processes, indicative of battery-like properties. Remarkably, the CV curve for NFT500 demonstrated a wider peak area and intensified peak currents, suggesting enhanced electrochemical behavior compared to the other tested electrodes, thus indicating superior capacitive properties. Galvanostatic charge–discharge (GCD) tests, conducted at 1 A g^{-1} and shown in Fig. S7b (ESI†), further validated the electrochemical reversibility of the electrodes. Of note, NFT500 exhibited an extended discharge duration relative to NFT300 and NFT600, affirming its higher energy storage capacity. The capacities for each material, displayed in Fig. S7c (ESI†), identified NFT500 as the most effective electrode, benefiting from its hollow structure that promotes more efficient ion transport and energy storage. Further comparative studies using CV were performed on Ni foam, Ni precursor, NiFeLDH, NFT500, and NFT@RGO at a scan rate of 10 mV s^{-1}, illustrated in Fig. 5a. Ni foam's CV trace showed a minimal area, indicating a lower capacitive

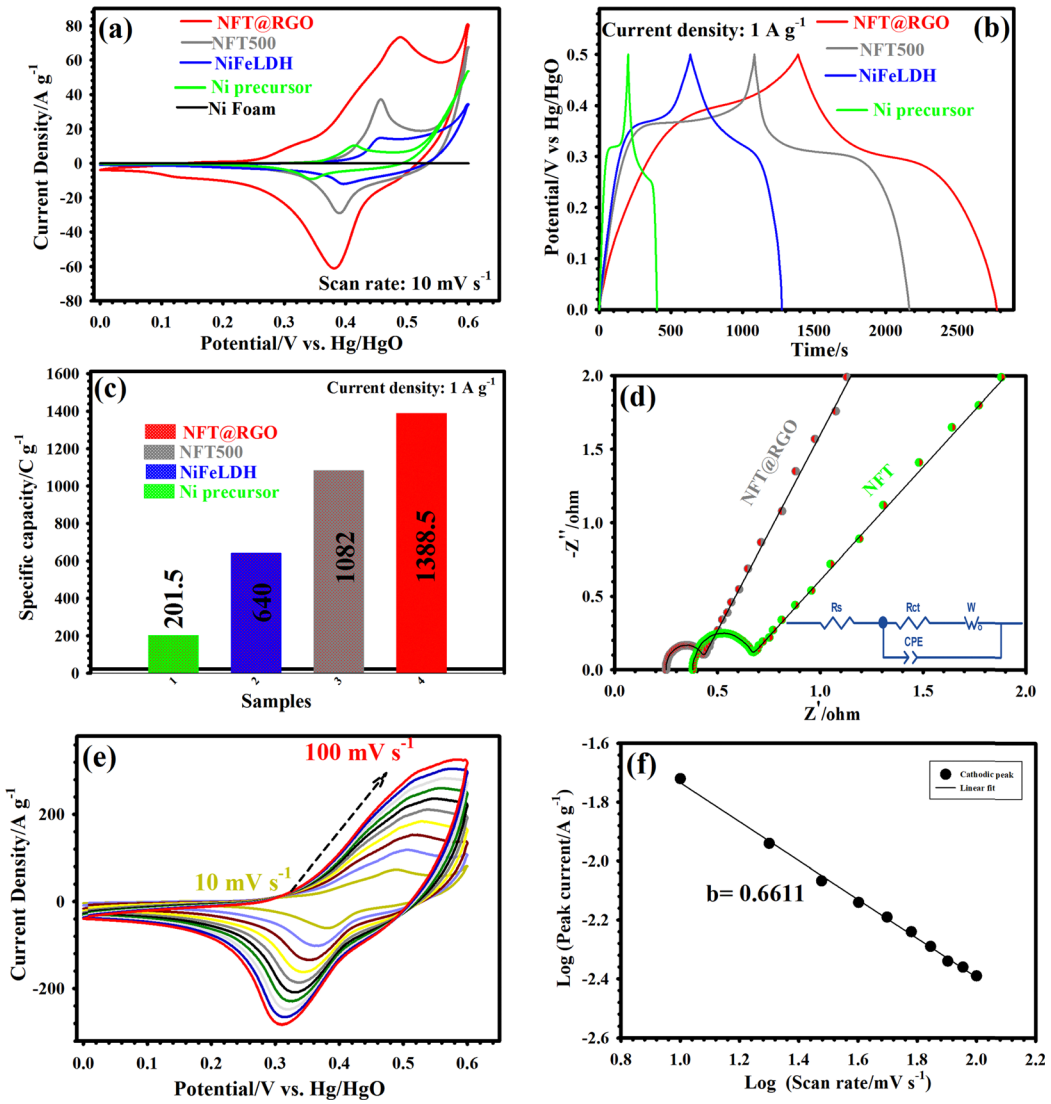

Fig. 5 (a) CV plots of the Ni foam, Ni precursor, NiFeLDH, NFT500, and NFT@RGO electrodes at 10 mV s^{-1}. (b) GCD plots of the Ni precursor, NiFeLDH, NFT500, and NFT@RGO electrodes at 1 A g^{-1}. (c) Specific capacities of the Ni precursor, NiFeLDH, NFT500, and NFT@RGO electrodes at 1 A g^{-1}. (d) Nyquist plots of the NFT500 and NFT@RGO electrodes (inset shows the equivalent circuit model). (e) CV plots of the NFT@RGO electrode from 10 to 100 mV s^{-1}. (f) Linear relation between the plot of the logarithm (i) *versus* logarithm (υ) of the NFT@RGO.

effect. In stark contrast, NFT@RGO presented an elevated current response, outperforming the other electrodes due to its substantial surface area and high porosity that enhance ion exchange rates and improve electrochemical kinetics.[23,42] Additionally, GCD evaluations aligned with the CV findings, conducted at 1 A g^{-1} for all materials, and presented in Fig. 5b. These results consistently showed that NFT@RGO maintained a longer discharge phase, indicating an enhanced capacity. The specific capacities, as recorded in Fig. 5c, reveal that NFT@RGO achieved a capacity of 1388.5 C g^{-1}, surpassing those of Ni precursor, NiFeLDH, and NFT500, which are 201.5, 640, and 1082 C g^{-1}, respectively. This superior performance by NFT@RGO is attributed to the RGO's contribution to conductivity and structural stability, which are essential for outstanding charge retention and cycling endurance.[45–47] To analyze the electrical resistance properties of the electrodes, Electrochemical Impedance Spectroscopy (EIS) was employed, with findings displayed in Fig. 5d. The Nyquist plots exhibited characteristic linear segments at lower frequencies, indicative of diffusion-controlled behavior, described as Warburg impedance.[52,53] Significantly, the plot for NFT@RGO showed a more acute inclination towards the *y*-axis, illustrating enhanced kinetics of electron–ion transport and heightened conductivity. This suggests that the combination of RGO's textural properties and the hollow structure of the material markedly boosts electron mobility across the electrode–electrolyte interface.[45,46] The analysis of these plots also helped determine the internal resistance (R_s) and charge transfer resistance (R_{ct}) of the electrodes. The intersection of the semicircle with the *x*-axis indicates R_s, whereas its diameter provides a measure of R_{ct}.[53] For NFT and NFTH@RGO, R_{ct} was measured at 0.49 Ω and 0.33 Ω, respectively, with R_s recorded at 0.38 Ω and 0.25 Ω, respectively.

The lower resistance values associated with NFT@RGO affirm the role of RGO in significantly boosting the conductivity and, consequently, the electrochemical efficacy of the nanoarchitectures.[23] Furthermore, the capacitive behavior of NFT@RGO was assessed using cyclic voltammetry (CV) at varying scan rates from 10 to 100 mV s^{-1}, detailed in Fig. 5e. The slight displacement of CV peaks is attributable to polarization effects.[45] Notably, an increase in the scan rate led to a proportional rise in current response for NFT@RGO, underscoring its exceptional charge rate capabilities.[14,19] CV results for other nanomaterials are compiled in Fig. S8 (ESI†). The faradaic reactions for the NFT are described by the following equations:[39]

$$Ni/FeTe + OH^- \leftrightarrow Ni/FeTeOH + e^- \quad (5)$$

$$Ni/FeTeOH + OH^- \leftrightarrow Ni/FeTeO + H_2O + e^- \quad (6)$$

A detailed kinetic study of these reactions in NFT@RGO was conducted by correlating peak current densities (I_p) with scan rates (ν), described by the equation.[46]

$$(I_p = a \times \nu^b) \quad (7)$$

In this equation, b and a represent constant, with ν denoting the scan rate and I the peak current. Electrodes with predominantly capacitive behavior exhibit a b value close to 1, while those demonstrating battery-like properties typically show b values around 0.5.[21,25] For NFT@RGO, the measured b value for the cathodic peak was 0.6611 (Fig. 5f), confirming a mixed capacitive and diffusion-controlled charge storage mechanism.

To emphasize the superior supercapacitive properties of NFT@RGO, GCD tests were conducted across a range of current densities from 1 to 30 A g^{-1}. The GCD curves for NFT@RGO, displayed in Fig. 6a, show exceptional symmetry, indicative of excellent coulombic efficiency. Compared with the other materials shown in Fig. S9 (ESI†), while potential plateaus on the GCD curves suggest a battery-like behavior, NFT@RGO's discharge durations were significantly longer than those of its counterparts. Detailed specific capacities for electrodes such as Ni precursor, NiFeLDH, NFT300, NFT500, NFT600, and NFT@RGO are precisely documented in Fig. 6b. NFT@RGO demonstrated outstanding capacities at different current densities, delivering 1388.5 C g^{-1} at 1 A g^{-1}, 1300 C g^{-1} at 2.5 A g^{-1}, 1221.5 C g^{-1} at 5 A g^{-1}, 1100 C g^{-1} at 15 A g^{-1}, and 1013.6 C g^{-1} at 30 A g^{-1}. In stark contrast, capacities at 1 A g^{-1} for other materials like Ni precursor, NiFeLDH, NFT300, NFT500, NFT600 were considerably lower, measured at 201.5, 640, 994, 1082, and 922 C g^{-1}, respectively. Remarkably, NFT@RGO retained 73% of its initial capacity even at a high current density of 30 A g^{-1},

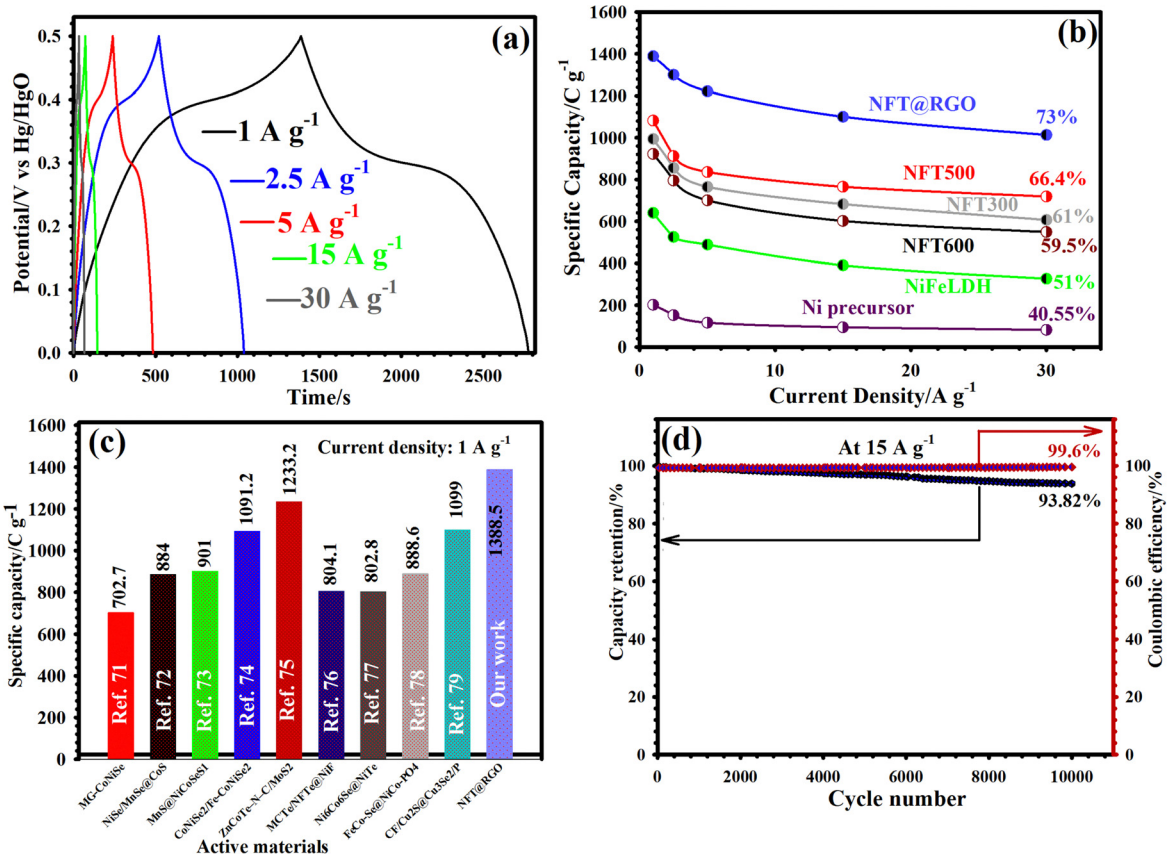

Fig. 6 (a) GCD plots of the NFT@RGO from 1 to 30 A g^{-1}. (b) Specific capacities *vs.* current densities of the Ni precursor, NiFeLDH, NFT600, NFT300, NFT500, and NFT@RGO electrodes. (c) Comparison of capacity values of the NFT@RGO with the previous literature. (d) Longevity and coulombic efficiency of the NFT@RGO at 15 A g^{-1} (inset shows the FESEM image of the NFT@RGO after cycling).

a retention rate significantly higher than that of Ni precursor (40.55%), NiFeLDH (51%), NFT300 (61%), NFT500 (66.4%), and NFT600 (59.5%). Further comparison of the NFT@RGO's capacity with previous nanomaterials emphasizes its notable efficiency and is indicated in Fig. 6c.[71–79] The superior performance of NFT@RGO is attributed to the synergistic effects between NFT and RGO within the composite. The incorporation of RGO enhances overall conductivity and surface area while introducing additional pseudocapacitive properties that significantly boost electrochemical efficiency.[23] This combination facilitates rapid electron–ion transfer through the structured cavities within the hollow NFT texture, leading to exceptional electrochemical performance.[42,45,46] Durability assessments involved continuous GCD cycling at 15 A g^{-1}, which demonstrated the robustness of these nanomaterials under operational stress. NFT@RGO exhibited an impressive capacity retention rate of 93.82% (Fig. 6d), substantially surpassing Ni precursor (30.8%), NiFeLDH (62.5%), and NFT500 (81%), as shown in Fig. S10 (ESI†). Additionally, it maintained a coulombic efficiency of 99.6% after the durability test, highlighting its excellent reversibility. Fig. S11 (ESI†) illustrates the initial and final 20 successive GCD cycles for the NFT@RGO composite. No significant alteration in the shape of the GCD curves was observed following the durability assessment, indicating exceptional cycling stability of the NFT@RGO material. Further validation of NFT@RGO's durability came from post-cycling EIS measurements. The Nyquist plot, depicted in Fig. S12 (ESI†), displayed only slight changes in electrical characteristics after extensive cycling, indicating remarkable stability. The post-cycling FESEM image, shown in Fig. S13 (ESI†), confirms the preservation of NFT@RGO's structural integrity, with no significant morphological degradation observed. The FESEM image of the NFT@RGO composite after 10 000 cycles shows some degree of structural degradation, which is expected due to the prolonged electrochemical stress. Despite this, the material retains 93.82% of its initial capacity, highlighting its exceptional cycling stability. The annotated FESEM image clearly identifies the remaining nanorod structures, providing insight into the material's post-cycling morphology. NFT@RGO's supercapacitive performance, compared with various previously reported electrodes, is extensively documented in ESI;† Table S1. This performance is enhanced by the integration of Te, which boosts conductivity and charge transport, the hollow structure that increases surface area, and the RGO network which prevents aggregation and improves electrolyte penetration, all contributing to superior ion diffusion speeds and reduced internal resistance. Further electrochemical examinations on AC revealed the electrochemical nature typical of electric double-layer capacitors (EDLCs), as highlighted by quasi-rectangular CV patterns and triangular GCD graphs, exhibited in Fig. S14a and b (ESI†). The capacitances for this material varied from 185.55 to 148.3 F g^{-1} from 1 to 30 A g^{-1}, respectively, as represented in Fig. S14c (ESI†).

The functionality of the developed nanomaterials was validated through the assembly of a hybrid device, employing AC as the negative electrode and NFT@RGO as the positive electrode, designated as the NFT@RGO//AC hybrid system (Fig. 7a). This setup broadened the operational voltage range of the cell to 1.60 V, incorporating the voltage windows of AC (−1.0 to 0.0 V) and NFT@RGO (0.0 to 0.60 V), corroborated by the CV profiles displayed in Fig. S15 (ESI†). Conducted at 10 mV s^{-1}, CV testing across the voltage range of 0 to 1.7 V (Fig. S16, ESI†) confirmed the stability within the 0–1.60 V interval. Deviations observed beyond 1.60 V indicated the beginnings of electrochemical instability at elevated voltages. Further CV analysis highlighted a progressive increase in current response with escalating scan rates (Fig. 7b), illustrating the hybrid device's robust electrochemical reversibility. The absence of distinct redox peaks in the hybrid supercapacitor's CV, despite the clear faradaic peaks in the positive electrode (NFT@RGO), can be explained by the following factors: (1) mutual contribution of both electrodes: the hybrid supercapacitor consists of a faradaic battery-type positive electrode (NFT@RGO) and a non-faradaic capacitive negative electrode (AC). The CV of the full device represents the combined response of both electrodes. While the positive electrode exhibits redox peaks in its individual CV, the symmetric, rectangular-shaped CV of the AC electrode (typical of EDLC behavior) dominates the overall response, masking the redox peaks in the full-cell measurement. (2) Kinetic and mass transport effects: in a hybrid configuration, the charge storage mechanisms of the two electrodes operate at different timescales. The fast, surface-dominated EDLC process (AC electrode) can overshadow the slower diffusion-controlled faradaic process (NFT@RGO), leading to a CV that appears more capacitive overall. Additionally, the higher mass loading and larger potential window of the AC electrode can further dilute the visibility of redox peaks. (3) Potential distribution and charge balancing: The operating voltage of the hybrid supercapacitor is shared between the two electrodes. Since the AC electrode covers a wide potential range with minimal polarization, the potential window allocated to the faradaic electrode may not be sufficient to fully resolve its redox peaks in the full-cell CV. Moreover, careful charge balancing between the electrodes (to maximize performance) can lead to a more smoothed-out CV curve. (4) Electrolyte and interface effects: the electrolyte ion mobility and interfacial resistance in the full cell can also influence the redox peak visibility. In a three-electrode setup (single electrode), the redox peaks are more pronounced due to unrestricted ion diffusion, whereas in the two-electrode full cell, ion transport limitations between the electrodes can broaden the peaks, making them less distinct. The device's electrochemical attributes were further assessed through GCD tests across a spectrum of current densities from 1 to 30 A g^{-1} (Fig. 7c). The resulting profiles, marked by their symmetrical nature, evidenced the device's exemplary coulombic efficiency. Capacities measured for the NFT@RGO//AC were 275 C g^{-1} at 1 A g^{-1}, 250 C g^{-1} at 2.5 A g^{-1}, 230.2 C g^{-1} at 5 A g^{-1}, 212.4 C g^{-1} at 15 A g^{-1}, and 193.2 C g^{-1} at 30 A g^{-1}, respectively, as delineated in Fig. 7d. Energy and power densities, vital metrics of supercapacitor performance, were represented on a Ragone plot (Fig. 7e), demonstrating an energy density of 61.11 W h kg^{-1} at a power density of 800.91 W kg^{-1}, which was sustained at 42.93 W h kg^{-1}

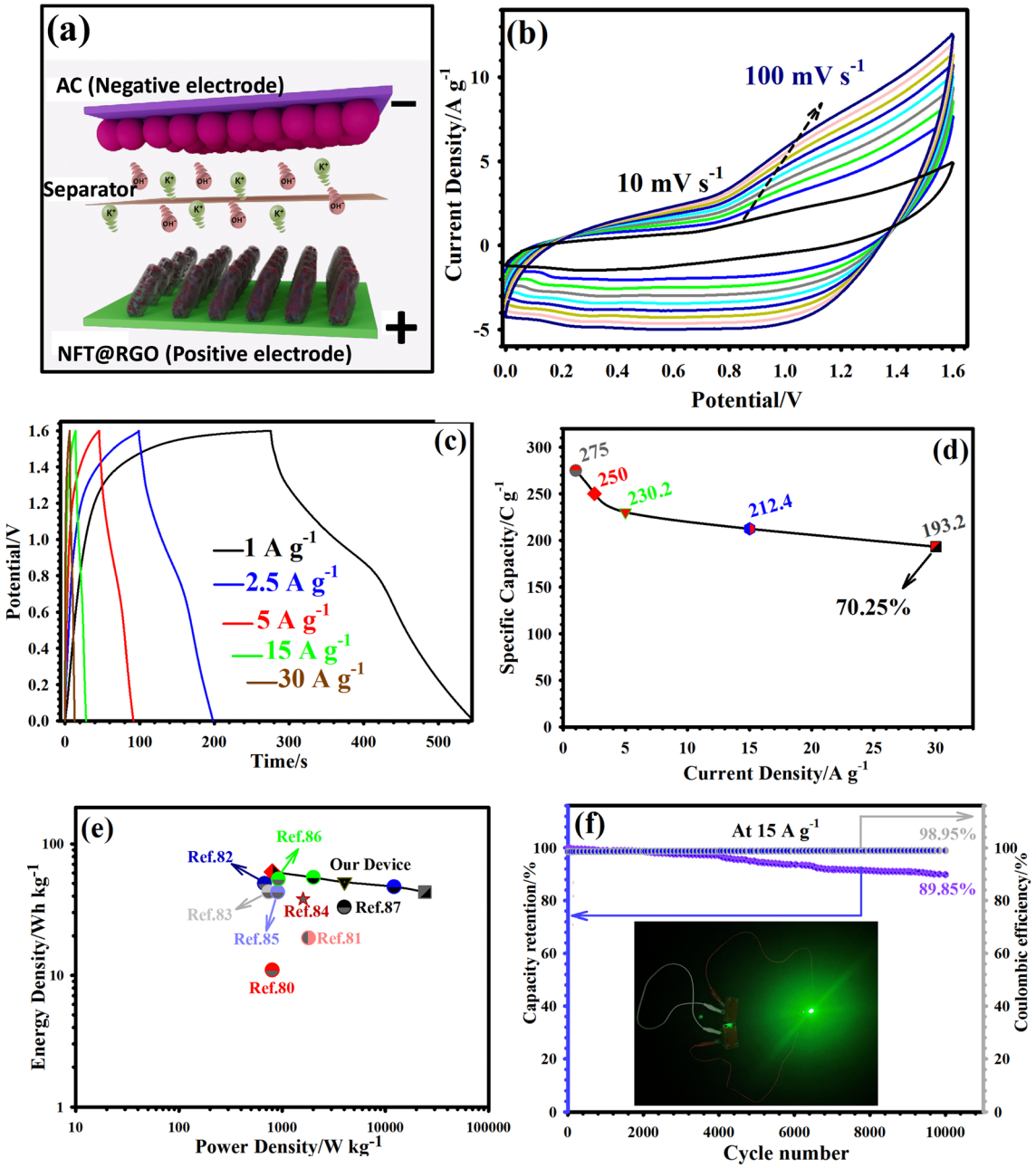

Fig. 7 (a) Schematic illustration of the NFT@RGO//AC. (b) CV curves of the NFT@RGO//AC from 10 to 100 mV s^{-1}. (c) GCD patterns of the NFT@RGO//AC from 1 to 30 A g^{-1}. (d) Specific capacity *vs.* current density of the NFT@RGO//AC. (e) The comparison of the AC//MZT@RGO device's Ragone plot with various devices. (f) Durability and coulombic efficiency of the NFT@RGO//AC at 15 A g^{-1} (the inset indicates the photograph of a LED with two NFT@RGO//AC devices).

even at a power density of 24 117.98 W kg^{-1}. These metrics notably surpass those of comparative cells, reinforcing the suitability of the NFT@RGO//AC for diverse applications (Fig. 7e and Table S1, ESI†).[80–87] Durability testing, conducted over 10 000 uninterrupted cycles at 15 A g^{-1} (Fig. 7f), verified the device's long-term stability, showing remarkable capacity retention along with high coulombic efficiencies of 89.85% and 98.95%. The practical application of the NFT@RGO//AC was demonstrated by powering a green lamp using two cells connected in series (Fig. 7f, inset and Video S1 in ESI†), effectively highlighting the device's capability for integration into real-world energy systems. The self-discharge rate is a critical performance metric for hybrid supercapacitors, as it directly impacts their practical applicability. Although often overlooked, this parameter plays a significant role in determining the long-term energy retention capability of such devices. To evaluate the self-discharge behavior of the NFT@RGO//AC device, two cells were charged to 1.6 V and then subjected to an open-circuit potential measurement over 1500 minutes at room temperature. As shown in Fig. S17 (ESI†), the device retained ~68% of its initial voltage after this

period, demonstrating a relatively slow self-discharge rate. Notably, even after 1500 minutes, the cell voltage remained above 1.0 V, indicating good energy retention and suggesting strong potential for real-world applications where prolonged charge storage is essential.

4. Conclusions

In this study, $NiTe_2$–$FeTe_2$ hollow nanorods (NFT) were successfully synthesized using a self-templated approach. To enhance the intrinsic supercapacitive performance of the NFT, these hollow rods were integrated into a reduced graphene oxide (RGO) matrix, resulting in the NFT@RGO nanocomposite. The hollow design, combined with the synergistic bimetallic interactions of Fe and Ni within the NFT structure, substantially increases the accessibility of electroactive sites and provides extensive channels for ion diffusion, thereby bolstering charge-transfer kinetics. Incorporating Te and a conductive RGO framework into the NFT@RGO composite further improves both the conductivity and the overall supercapacitive performance. Electrochemical evaluations revealed that the NFT@RGO-based electrode delivers excellent efficiency and stability. Moreover, when assembled into a hybrid device with activated carbon (AC) as the negative electrode (NFT@RGO//AC), the device achieves an energy density of 61.11 W h kg^{-1} at a power density of 800.91 W kg^{-1} and retains 89.85% of its capacity over extended cycles. These findings confirm the strong potential of NFT@RGO in applications demanding both high energy density and long operational lifetimes. The unique nanoarchitecture of NFT@RGO coupled with the synergistic effects of RGO, Te, and the bimetallic hollow rods positions this material as a compelling candidate for next-generation energy storage technologies.

Data availability

The data supporting this article have been included as part of the ESI.†

Conflicts of interest

The authors declare no competing financial interest.

Acknowledgements

The authors gratefully acknowledge the support of this work by Research councils of Shahid Beheshti University and Iranian Research Organization for Science and Technology.

References

1 M. A. Saghafizadeh, A. Mohammadi Zardkhoshoui, B. Ameri and S. S. Hosseiny Davarani, *Chem. Eng. J.*, 2025, **508**, 160817.
2 X. Yang, C. Hu, Y. Chen, Z. Song, L. Miao, Y. Lv, H. Duan, M. Liu and L. Gan, *J. Energy Storage*, 2024, **104**, 114509.
3 Y. Chen, Z. Song, Y. Lv, L. Gan and M. Liu, *Nano-Micro Lett.*, 2025, **17**, 117.
4 D. Zhang, L. Miao, Z. Song, X. Zheng, Y. Lv, L. Gan and M. Liu, *Energy Fuels*, 2024, **38**, 12510–12527.
5 S. Kour, P. Koura and A. L. Sharma, *Nanoscale*, 2024, **16**, 21456–21470.
6 A. Mohammadi Zardkhoshoui, G. R. Rostami and S. S. Hosseiny Davarani, *Energy Fuels*, 2024, **38**, 21498–21509.
7 M. Molaei, M. Abdollahi, A. Mohammadi Zardkhoshoui and S. S. Hosseiny Davarani, *J. Energy Storage*, 2024, **85**, 111079.
8 H. Gholami Shamami, A. Mohammadi Zardkhoshoui and S. S. Hosseiny Davarani, *Nanoscale*, 2025, **17**, 4591–4602.
9 S. D. Sutar and A. Swami, *Nanoscale*, 2025, **17**, 4750–4764.
10 N. Karimipour, A. Mohammadi Zardkhoshoui and S. S. Hosseiny Davarani, *J. Energy Storage*, 2025, **114**, 115801.
11 A. Mohammadi Zardkhoshoui, B. Ameri and S. S. Hosseiny Davarani, *Chem. Eng. J.*, 2022, **435**, 135170.
12 G. Li, H. Cai, X. Li, J. Zhang, D. Zhang, Y. Yang and J. Xiong, *ACS Appl. Mater. Interfaces*, 2019, **11**, 37675–37684.
13 W. Zhang, C. Xu, C. Ma, G. Li, Y. Wang, K. Zhang, F. Li, C. Liu, H.-M. Cheng, Y. Du, N. Tang and W. Ren, *Adv. Mater.*, 2017, **29**, 1701677.
14 A. Mohammadi Zardkhoshoui, B. Ameri and S. S. Hosseiny Davarani, *Chem. Eng. J.*, 2021, **422**, 129953.
15 S. Liu, Y. Yin, Y. Shen, K. S. Hui, Y. T. Chun, J. M. Kim, K. N. Hui, L. Zhang and S. C. Jun, *Small*, 2020, **16**, 1906458.
16 Z. Pan, L. Jin, C. Yang, X. Ji and M. Liu, *Chem. Eng. J.*, 2023, **470**, 144084.
17 F. Song, G. Yang, L. Pan and Q. Chen, *Composites, Part B*, 2023, **267**, 111025.
18 Q. Wu, F. Li, H. Sheng, Y. Qi, J. Yuan, H. Bi, W. Li, E. Xie and W. Lan, *ACS Appl. Mater. Interfaces*, 2024, **16**, 23241–23252.
19 M. Molaei, G. R. Rostami, A. Mohammadi Zardkhoshoui and S. S. Hosseiny Davarani, *J. Colloid Interface Sci.*, 2024, **653**, 1683–1693.
20 H. Wang, X. Gao, Y. Xie, E. Guo, H. Bai, F. Jiang, Q. Li and H. Yue, *Adv. Energy Mater.*, 2024, **7**, 2400493.
21 D. Dehghanpour Farashah, F. Beigloo, A. Mohammadi Zardkhoshoui and S. S. Hosseiny Davarani, *Chem. Eng. J.*, 2023, **474**, 145584.
22 W. Lu, J. Shen, P. Zhang, Y. Zhong, Y. Hu and X. Lou, *Angew. Chem.*, 2019, **131**, 15587–15593.
23 A. Mohammadi Zardkhoshoui, B. Ameri and S. S. Hosseiny Davarani, *Chem. Eng. J.*, 2023, **470**, 144132.
24 P. Zhang, B. Y. Guan, L. Yu and X. W. Lou, *Angew. Chem., Int. Ed.*, 2017, **129**, 7247–7251.
25 D. Dehghanpour Farashah, F. Beigloo, A. Mohammadi Zardkhoshoui and S. S. Hosseiny Davarani, *Sustainable Energy Fuels*, 2023, **7**, 4922–4934.
26 B. Ameri, A. Mohammadi Zardkhoshoui and S. S. Hosseiny Davarani, *Mater. Chem. Front.*, 2021, **5**, 4725–4738.
27 A. Mohammadi Zardkhoshoui and S. S. Hosseiny Davarani, *Chem. Eng. J.*, 2020, **402**, 126241.
28 H. Liu, X. Liu, S. Wang, H.-K. Liu and L. Li, *Energy Storage Mater.*, 2020, **28**, 122–145.

29 T. Nguyen and M. D. F. Montemor, *Adv. Sci.*, 2019, **6**, 1801797.
30 G. B. Bhanuse, S. Kumar, C.-C. Yu and Y.-P. Fu, *ACS Appl. Nano Mater.*, 2024, **7**, 13649–13663.
31 J. Jiang, X. Huang, R. Sun, X. Chen and S. Han, *J. Colloid Interface Sci.*, 2023, **640**, 662–679.
32 C. Guan, X. Liu, W. Ren, X. Li, C. Cheng and J. Wang, *Adv. Energy Mater.*, 2017, **7**, 1602391.
33 Z. Tian, K. Zhou, M. Xie, Y. Zhang, J. Chen, C. Du and L. Wan, *Chem. Eng. J.*, 2022, **447**, 137495.
34 S. Li, S. Wang and J. Wang, *J. Colloid Interface Sci.*, 2022, **617**, 304–314.
35 G. Zhang, Y. Xu, Z. Ma, J. Liu, Y. Luo, J. Wang, W. Li, H. Yang and X. Li, *J. Energy Chem.*, 2023, **71**, 108138.
36 M. Pathak, P. Mane, B. Chakraborty, J. Cho, S. Jeong and C. S. Rout, *Small*, 2024, **20**, 2310120.
37 C. Debbarma, S. Radhakrishnan, S. M. Jeong and C. S. Rout, *J. Mater. Chem. A*, 2024, **12**, 18674–18704.
38 D. Dehghanpour Farashah, M. Abdollahi, A. Mohammadi Zardkhoshoui and S. S. Hosseiny Davarani, *Nanoscale*, 2024, **16**, 8650–8660.
39 C. Shi, Q. Yang, S. Chen, Y. Xue, Y. Hao and Y. Yan, *ACS Appl. Energy Mater.*, 2022, **5**, 2817–2825.
40 J. Zhou, Y. Wang, L. Chen, W. Zhao and L. Han, *Dalton Trans.*, 2023, **52**, 12978–12987.
41 A. Mohammadi Zardkhoshoui, B. Ameri and S. S. Hosseiny Davarani, *Nanoscale*, 2021, **13**, 2931–2945.
42 A. Mohammadi Zardkhoshoui and S. S. Hosseiny Davarani, *Nanoscale*, 2020, **12**, 12476–12489.
43 T. Liu, L. Zhang, W. You and J. Yu, *Small*, 2018, **14**, 1702407.
44 X. Zhao, Q. Bi, C. Yang, K. Tao and L. Han, *Dalton Trans.*, 2021, **50**, 15260–15266.
45 A. Mohammadi Zardkhoshoui and S. S. Hosseiny Davarani, *Nanoscale*, 2020, **12**, 1643–1656.
46 B. Ameri, A. Mohammadi Zardkhoshoui and S. S. Hosseiny Davarani, *Mater. Chem. Front.*, 2023, **7**, 3127–3145.
47 M. Amiri, A. Mohammadi Zardkhoshoui and S. S. Hosseiny Davarani, *Nanoscale*, 2023, **15**, 2806–2819.
48 L. Teng, J. Duan, H. Liu, X. Zhang, J. Li, Y. Li, J. Hong, W. Lyu and Y. A. Liao, *J. Mater. Chem. A*, 2024, **12**, 12423–12434.
49 L. Yan, C. Shen, L. Niu, M.-C. Liu, J. Lin, T. Chen, Y. Gong, C. Li, X. Liu and S. Xu, *ChemSusChem*, 2019, **12**, 3571–3581.
50 M.-C. Liu, Y. Xu, Y.-X. Hu, Q.-Q. Yang, L.-B. Kong, W.-W. Liu, W.-J. Niu and Y.-L. Chueh, *ACS Appl. Mater. Interfaces*, 2018, **10**, 35571–35579.
51 X. Yang, Y. Tian, S. Li, Y.-P. Wu, Q. Zhang, D.-S. Li and S. Zhang, *J. Mater. Chem. A*, 2022, **10**, 12225–12234.
52 B. Ameri, A. Mohammadi Zardkhoshoui and S. S. Hosseiny Davarani, *Dalton Trans.*, 2021, **50**, 8372–8384.
53 S. C. Sekhar, B. Ramulu, S. J. Arbaz, S. K. Hussain and J. S. Yu, *Small Methods*, 2021, **5**, 2100335.
54 L. Wan, Y. Wang, Y. Zhang, C. Du, J. Chen, Z. Tian and M. Xie, *Chem. Eng. J.*, 2021, **415**, 128995.
55 S. K. Hussain, G. Nagaraju, S. C. Sekhar and J. S. Yu, *J. Power Sources*, 2019, **439**, 227088.
56 L. He, P. Cai, H. Lai, K. Lu, Z. Xu, R. Zeng, C. Hao, Z. Wang and W. Gan, *Chem. Eng. J.*, 2025, **504**, 159149.
57 K. R. Kumar, N. D. Sri, V. N. Kale and T. Maiyalagan, *Int. J. Hydrogen Energy*, 2025, **101**, 837–847.
58 Z. Lin, H. Zhang, C. Yang, Z. Liu, D. Wen, X. Peng, S. Li and X. Wu, *Sustainable Energy Fuels*, 2024, **8**, 934–941.
59 K. C. Majhi and M. Yadav, *Int. J. Hydrogen Energy*, 2020, **45**, 24219–24231.
60 J. Guo, Y. Shi, Y. Chu and T. Ma, *Chem. Commun.*, 2013, **49**, 10157–10159.
61 L. Kulandaivel, J. W. Park, P. Sivakumar and H. Jung, *J. Mater. Sci.: Mater. Electron.*, 2023, **34**, 1557.
62 S. Nappini, D. W. Boukhvalov, G. D'Olimpio, L. Zhang, B. Ghosh, C.-N. Kuo, H. Zhu, J. Cheng, M. Nardone, L. Ottaviano, D. Mondal, R. Edla, J. Fuji, C. S. Lue, I. Vobornik, J. A. Yarmoff, A. Agarwal, L. Wang, L. Zhang, F. Bondino and A. Politano, *Adv. Funct. Mater.*, 2020, **30**, 2000915.
63 B. P. Jena and C. Sudakar, *ACS Appl. Nano Mater.*, 2024, **7**, 26215–26225.
64 M. Amiri, A. Mohammadi Zardkhoshoui, S. S. Hosseiny Davarani, M. Maghsoudi and M. K. Altafi, *Sustainable Energy Fuels*, 2022, **6**, 3626–3642.
65 Y. A. Haj, J. Balamurugan, N. H. Kim and J. H. Lee, *J. Mater. Chem. A*, 2019, **7**, 3941–3952.
66 B. Hu, X. Liu, A. Liu, Y. Ren, Z. Guo, J. Mu, X. Zhang, Z. Zhang, X. Liu and H. Che, *ACS Appl. Nano Mater.*, 2021, **4**, 13267–13278.
67 W. Yao, C. Tian, C. Yang, J. Xu, Y. Meng, I. Manke, N. Chen, Z. Wu, L. Zhan, Y. Wang and R. Chen, *Adv. Mater.*, 2022, **34**, 2106370.
68 Z. Li, F. Yu, X. Yang, Y. Yang, X. Li, Y. Gao, L. Wang and W. Lü, *Chem. Eng. J.*, 2025, **504**, 159100.
69 Y. Guo, Y. Cheng, Q. Li and K. Chu, *J. Energy Chem.*, 2021, **56**, 259–263.
70 S. Zhang, L. Qiu, Y. Zheng, Q. Shi, T. Zhou, V. Sencadas, Y. Xu, S. Zhang, L. Zhang, C. Zhang, C.-L. Zhang, S.-H. Yu and Z. Guo, *Adv. Funct. Mater.*, 2021, **31**, 2006425.
71 J. Chen, T. Song, M. Sun, S. Qi, C. Chen, Y. Zhao and X. Wu, *J. Alloys Compd.*, 2024, **1009**, 176786.
72 L. Wan, G. Ye, Y. Zhang, J. Chen, C. Du and M. Xie, *Appl. Surf. Sci.*, 2024, **670**, 160638.
73 H. Ren, H. Guo, Y. Hao, Y. Liu, L. Peng and W. Yang, *J. Colloid Interface Sci.*, 2025, **683**, 746–758.
74 Z. Andikaey, A. A. Ensafi, B. Rezaei and J.-S. Hu, *Electrochim. Acta*, 2022, **417**, 140338.
75 M. B. Poudel, A. R. Kim, S. Ramakrishan, N. Logeshwaran, S. K. Ramasamy, H. J. Kim and D. J. Yoo, *Composites, Part B*, 2022, **247**, 110339.
76 T. S. Panah, M. Shirvani and S. S. Hosseiny Davarani, *J. Colloid Interface Sci.*, 2025, **678**, 1012–1024.
77 D. Khalafallah, W. Huang, M. Zh and Z. Hong, *Energy Environ. Mater.*, 2024, **7**, e12528.
78 K. Yang, H. Zhu, L. Zhang, W. Li and L. Sun, *ACS Appl. Mater. Interfaces*, 2024, **16**, 66138–66148.
79 H. Fu, A. Zhang, H. Guo, L. Duan, F. Jin, H. Zong, X. Sun and J. Liu, *ACS Appl. Mater. Interfaces*, 2023, **15**, 8169–8180.
80 G. P. Patil, C. D. Jadhav, S. Lyssenko and R. Minnes, *Chem. Eng. J.*, 2024, **498**, 155284.

81 H. K. Rathore, M. Hariram, M. K. Ganesha, A. K. Singh, D. Das, M. Kumar, K. Awasthi and D. Sarkar, *J. Colloid Interface Sci.*, 2022, **621**, 110–118.
82 P. Bhol, S. A. Patil, N. Barman, E. E. Siddharthan, R. Thapa, M. Saxena, A. Altaee and A. K. Samal, *Mater. Today Chem.*, 2023, **30**, 101557.
83 T. Kshetri, T. I. Singh, Y. S. Lee, D. D. Khumujam, N. H. Kim and J. H. Lee, *Composites, Part B*, 2021, **211**, 108624.
84 W. Younas, M. K. Tufail, N. Mushtaq, L. Wang, P. He, J. Tang and Q. Liu, *J. Energy Storage*, 2024, **101**, 113860.
85 M. Manikandan, K. Subramani, S. Dhanuskodi and M. Sathish, *Energy Fuels*, 2021, **35**, 12527–12537.
86 S. Zhang, D. Yang, M. Zhang, Y. Liu, T. Xu, J. Yang and Z.-Z. Yu, *Inorg. Chem. Front.*, 2020, **7**, 477–486.
87 B. Ye, M. Huang, Q. Bao, S. Jiang, J. Ge, H. Zhao, L. Fan, J. Lin and J. Wu, *ChemElectroChem*, 2018, **5**, 507–514.